

Topo-R1: Detecting Topological Anomalies via Vision-Language Models

Meilong Xu¹, Qingqiao Hu¹, Xiaoling Hu², Shahira Abousamra³, Xin Yu⁴,
Weimin Lyu¹, Kehan Qi¹, Dimitris Samaras¹, and Chao Chen¹

¹ Stony Brook University, Stony Brook, NY, USA

² Massachusetts General Hospital and Harvard Medical School, MA, USA

³ Department of Biomedical Data Science, Stanford University, CA, USA

⁴ Penn State University, PA, USA

Abstract. Topological correctness is crucial for tubular structures such as blood vessels, nerve fibers, and road networks. Existing topology-preserving methods rely heavily on domain-specific ground truth, which is costly to produce and rarely transfers across domains. When deployed to a new domain without annotations, a pressing question arises: how can we detect topological anomalies without ground-truth supervision? We reframe this as topological anomaly detection, a structured visual reasoning task in which a model needs to locate and classify topological errors in a predicted segmentation mask. Vision-Language Models (VLMs) are natural candidates for this task; however, we find that both state-of-the-art closed-source and open-source VLMs perform almost at random, as they lack the fine-grained, topology-aware perception capabilities needed to identify sparse connectivity errors in densely connected structures. To bridge this gap, we first develop an automated data-curation pipeline that synthesizes diverse topological anomalies with verifiable annotations across graduated difficulty levels, enabling us to construct the first large-scale, multi-domain benchmark for topological anomaly detection. Using the curated training data, we introduce **Topo-R1**, a framework that endows VLMs with topology-aware perception via a two-stage training paradigm: supervised fine-tuning followed by reinforcement learning with Group Relative Policy Optimization (GRPO). Central to our approach is a topology-aware composite reward designed specifically for this task, which integrates type-aware Hungarian matching for structured error classification, spatial localization scoring, and a centerline Dice (clDice) reward that directly penalizes connectivity disruptions in predicted anomaly regions, thereby jointly incentivizing both semantic precision and structural fidelity. Extensive experiments demonstrate that **Topo-R1** establishes a new paradigm for annotation-free topological quality assessment, consistently outperforming both general-purpose VLMs and supervised baselines across all evaluation protocols.

Keywords: Topological Data Analysis, Anomaly Detection, Vision Language Model

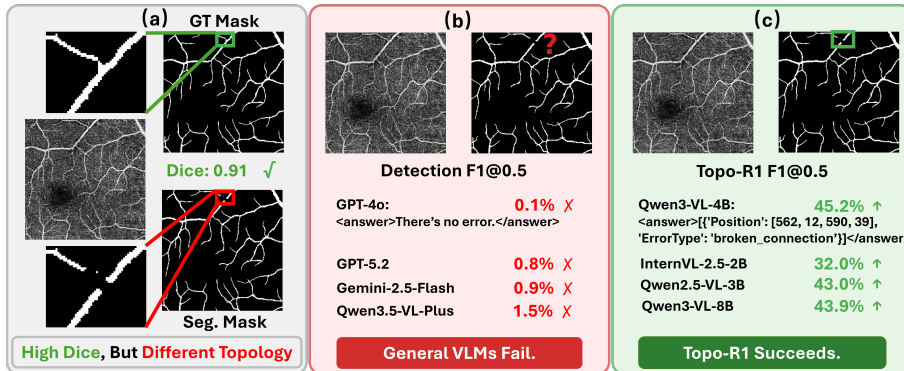


Fig. 1: Intuition of the framework. (a) A segmentation mask can achieve a high pixel-wise Dice score (0.91) yet contain critical topological errors, such as broken or spurious connections, that are visible only upon close structural inspection. (b) State-of-the-art VLMs, including GPT-5.2 and Gemini-2.5-Flash, fail to detect these topological anomalies (near-zero Detection F1@0.5). (c) Topo-R1 successfully detects and classifies the topological error with structured, typed bounding-box outputs.

1 Introduction

Tubular structures, such as blood vessels, nerve fibers, and road networks, underlie biological systems and human infrastructure [26, 33, 51, 59, 76]. While attributes such as thickness and topology contribute to the functional analysis of these structures, topology plays a uniquely critical role: connectivity, branching patterns, and loop structure directly govern blood flow, neural signaling, and route planning. A single missing pixel can sever a vessel and invalidate a hemodynamic simulation; a spurious bridge between two road segments can corrupt an entire navigation graph. Existing topology-preserving segmentation methods [13, 25, 26, 76, 80] have made significant progress, yet they fundamentally rely on supervised training with pixel-level ground-truth annotations. Although recent works have begun exploring topology-aware learning with unlabeled data in semi-supervised settings [93, 94], these approaches still require a labeled subset within the same domain. Producing topologically correct annotations requires specialized domain expertise and is extremely time-consuming. The large domain gap across application areas (e.g., retinal vasculature, road networks, neural circuits) means that annotations from one domain rarely transfer to another. When deploying to a new domain where ground truth is unavailable, a critical question arises: how can we identify potential topological errors without domain-specific supervision? A model capable of automatically detecting such anomalies would enable quality assurance for existing pipelines, allowing experts to efficiently verify outputs and flag regions for correction, and further facilitating self-training and active learning across domains.

A natural candidate for topology-aware perception are VLMs such as GPT-4o [29], Gemini [23], LLaVA [47, 48], Qwen-VL [3, 4, 84, 88], InternVL [11], and Molmo [17], given their strong capabilities across visual question answering,

grounding, and spatial reasoning [39, 58, 101]; however, our extensive evaluation reveals that both leading closed-source and state-of-the-art open-source VLMs perform almost randomly on topological anomaly detection, as shown in Fig. 1. Even with carefully designed prompts and in-context examples, these models consistently fail to identify **localized yet important connectivity changes**, such as a few missing pixels that sever a vessel or a thin bridge that wrongly merges two road segments. This is due to limitations in both training data and training methodology. First, public-domain VLMs are typically pre-trained on data emphasizing medium- and large-scale visual patterns, with virtually no training signal for topology-aware perception of fine-grained structural details [10, 32, 85].

More fundamentally, topology-aware perception is inherently challenging because tubular networks form densely connected graphs in which anomalies are extremely sparse and localized: a single missing pixel among thousands of correctly segmented pixels can break a critical connection. Detecting such errors requires the model to efficiently search this vast, mostly correct structure and identify the few points where connectivity changes, a needle-in-a-haystack problem that standard VLMs have no mechanism to solve. Unlike object detection where salient visual cues guide attention, topological errors are often visually subtle and can only be recognized by tracing long-range connectivity across the entire network, demanding a combination of global structural reasoning and fine-grained local perception that current architectures lack. Without targeted training that helps the model focus on the right regions, VLMs cannot bridge the gap between pixel-level perception and topological understanding.

To bridge this gap, we introduce **Topo-R1**, the first framework to incorporate topology-aware perception into VLMs. We reframe topological anomaly detection as a structured visual reasoning task: given an image paired with a binary mask of a tubular network, the model must locate every region containing a topological error and classify it into one of four structural categories (see definitions in Sec. 3.2). Training a VLM for this task is fundamentally challenging. A natural starting point is supervised fine-tuning (SFT), which bootstraps the model from near-random baseline performance. However, as shown in Fig. 2, SFT alone yields limited gains: its maximum-likelihood objective lacks the exploration needed to handle the sparse and needle-in-a-haystack anomaly signals.

To enable the model to explore a much wider solution space and discover sparse topological anomalies that SFT misses, we adopt Group Relative Policy Optimization (GRPO) [72], a reinforcement learning strategy that generates

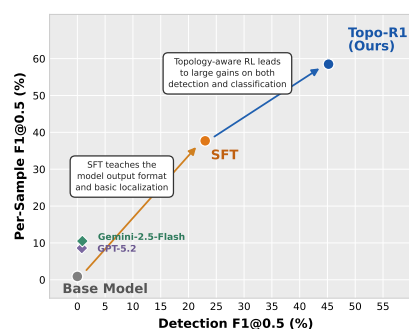


Fig. 2: The performance of state-of-the-art VLMs and our Topo-R1 on the topological anomaly detection task.

multiple candidate predictions per input and reinforces the better ones through relative ranking. Crucially, the effectiveness of RL hinges on what the reward measures. We design a topology-specific composite reward that simultaneously teaches the model two things: *where* an error occurs and *what type* it is. The reward independently credits correct localization and classification, and further incorporates a centerline-aware component inspired by cIDice [76] that activates only when the error type is correctly identified, steering the model to focus on the topologically critical skeleton rather than superficial pixel overlap. This reward design encodes the key insight that topological errors are defined by their effects on connectivity, not by the number of pixels they occupy, thereby giving the RL policy the right inductive bias to learn meaningful topology-aware perception.

In summary, our contributions are threefold:

1. We present the first vision-language approach to topological anomaly detection and classification on tubular structures. We show that existing VLMs, including state-of-the-art closed-source models, lack topology-aware perception, and introduce **Topo-R1**, a framework that incorporates this capability through topology-aware training.
2. We develop a fully automated, multi-domain data curation pipeline that aggregates data from multiple sources and injects four types of controlled topological anomalies with automated verification, yielding the first large-scale benchmark of over 4k annotated samples for topological anomaly detection and over 60k samples for training. Both the pipeline and the benchmark will be publicly released.
3. We design a composite reward system that integrates a decoupled accuracy reward, separately scoring error-type classification and bounding-box localization, with a novel type-conditioned cIDice reward that measures skeleton-level overlap to guide the model toward topologically significant regions. Experiments demonstrate that Topo-R1 substantially outperforms all baseline VLMs across multiple detection metrics.

2 Related Work

Topology-Driven Deep Image Analysis. Tubular structure segmentation has evolved from hand-crafted filters [22] and encoder-decoder architectures [30, 60, 69, 103] to topology-aware losses such as persistent-homology penalties [6, 26, 93, 94], cIDice [76], Skeleton Recall [34], homotopy warping [25], Betti matching [56, 79, 80], and Euler-characteristic optimisation [43]; Decroocq et al. [16] benchmark these metrics comprehensively. All such methods shape the training loss to prevent topological errors but do not reason about where each error occurs or what type it is. For *post-hoc* assessment, Li et al. [42, 44] detect violations via Euler Characteristic maps, yet produce only pixel-level heatmaps without structured, typed detections and remain coupled to specific CNN backbones. Our work instead formulates topological anomaly detection as a structured visual reasoning task with typed bounding-box output.

VLMs for Visual Understanding and Inspection. Vision-Language Models (VLMs) align visual encoders with LLMs via contrastive pretraining [66], cross-attention [1], bridging modules [15,40], and visual instruction tuning [47,48,104], yielding systems such as Qwen-VL [3,4], InternVL [11], CogVLM [89], GPT-4V [61], and Gemini [23]. Grounding-oriented models [9,49,64,96] add region-level perception, and domain-specific adaptations address biomedical VQA [39] and reasoning-based segmentation [36]. A parallel line applies VLMs as visual quality inspectors: AnomalyGPT [24] and MMAD [31] target industrial anomaly detection; Anomaly-OneVision [92] and AnomalyR1 [8] extend this to zero-shot and RL-based settings; and ConnectomeBench [7] benchmarks LLMs on neuron segmentation proofreading but provides only a 3D benchmark, not a trainable detector for 2D tubular topology errors. Our work addresses this gap by introducing a VLM that detects and classifies topological defects using structured bounding-box outputs.

Reinforcement Fine-Tuning in Visual Context. RL-based alignment has evolved from RLHF with PPO [12,62,71] and preference methods [2,19,67] to GRPO [72], which enables compact visual reasoning models [21,28,83,90,95,100] to rival larger supervised counterparts, with stability improvements from Hint-GRPO [27] and VL-Rethinker [87]. For fine-grained perception, Visual-RFT [55] pioneered IoU-based rewards; Seg-Zero [53], VisionReasoner [54], and LENS [105] extend RL to segmentation; VLM-R1 [74] and Perception-R1 [97] highlight reward design as the pivotal factor; and grounding emerges from answer-correctness rewards alone [5,20,70,73]. Medical adaptations [37,63,81,91] apply GRPO to visual reasoning and grounding, while preference-based alternatives [41,82,86,98,99] target hallucination reduction. Despite these advances, no prior work applies RL fine-tuning to topological quality assessment. We bridge this gap with a composite GRPO reward that incorporates a type-aware centerline Dice component and a domain-specific formulation unexplored in prior visual RL.

3 Method

In this section, we will introduce our **Topo-R1** framework in detail.

3.1 Preliminaries

Topological Data Analysis. Topological data analysis (TDA) provides algebraic tools for characterizing the shape and connectivity of data [18]. Central to TDA are the *Betti numbers*, which summarize the rank of homology groups across dimensions. For a topological space X , the k -th Betti number $\beta_k = \text{rank } H_k(X)$ counts the number of independent k -dimensional holes: β_0 counts connected components, β_1 counts loops or tunnels, and β_2 counts enclosed cavities. In biomedical image segmentation, these invariants provide a structure-aware characterization that complements pixel-level metrics. For instance, in tubular network segmentation, β_0 reflects the number of disjoint vessel

fragments while β_1 captures the presence of closed loops, making Betti-number errors a natural proxy for topological correctness [26, 80].

Group Relative Policy Optimization. Supervised fine-tuning (SFT) optimizes the standard next-token prediction objective: $\mathcal{L}_{\text{SFT}} = -\sum_{t=1}^T \log \pi_{\theta}(y_t | x, y_{<t})$, where x denotes the input (image and prompt), $y = (y_1, \dots, y_T)$ is the target response, and π_{θ} is the policy parameterized by θ . This token-level likelihood is a proxy objective that does not directly capture downstream goals such as precise localization and accurate type classification. We therefore refine the model with reinforcement learning, adopting Group Relative Policy Optimization (GRPO) [72], which forgoes a separate critic network by estimating advantages from within-group reward statistics.

Given a query q , the policy π_{θ} samples a group of G candidate outputs $\{o_1, \dots, o_G\}$. Each output is scored by the composite reward function described in Sec. 3.3, yielding scalar rewards $\{R_1, \dots, R_G\}$. The advantage for the i -th output is obtained by standardizing within the group:

$$\hat{A}_i = \frac{R_i - \mu_G}{\sigma_G + \epsilon_{std}}, \quad (1)$$

where $\mu_G = \frac{1}{G} \sum_{j=1}^G R_j$ and $\sigma_G = \sqrt{\frac{1}{G} \sum_{j=1}^G (R_j - \mu_G)^2}$ denote the group mean and standard deviation, respectively. The policy is then updated by maximizing the GRPO objective, which couples the clipped surrogate loss from PPO [71] with a KL-divergence penalty that anchors π_{θ} to a reference policy π_{ref} (initialized from the SFT checkpoint):

$$\mathcal{J}_{\text{GRPO}}(\theta) = \mathbb{E}_{q \sim \mathcal{D}, \{o_i\} \sim \pi_{\theta_{\text{old}}}(\cdot | q)} \left[\frac{1}{G} \sum_{i=1}^G L_i^{\text{clip}} - \beta D_{\text{KL}}(\pi_{\theta} \| \pi_{\text{ref}}) \right], \quad (2)$$

with the per-sample clipped surrogate defined as

$$L_i^{\text{clip}} = \min \left(r_i(\theta) \hat{A}_i, \text{clip}(r_i(\theta), 1-\epsilon, 1+\epsilon) \hat{A}_i \right), \quad (3)$$

where $r_i(\theta) = \pi_{\theta}(o_i | q) / \pi_{\theta_{\text{old}}}(o_i | q)$ is the importance-sampling ratio, with θ_{old} denoting the policy parameters from the previous iteration. The clipping threshold ϵ bounds the policy update to prevent excessively large steps, while β controls the strength of the KL regularization.

3.2 Automated Data Curation Pipeline

Manual annotation of topological errors demands expert knowledge and is prohibitively costly at scale. We therefore develop a fully automated pipeline that generates synthetic training data by injecting controlled topological anomalies into clean segmentation masks. The overall pipeline is shown in Fig. 3.

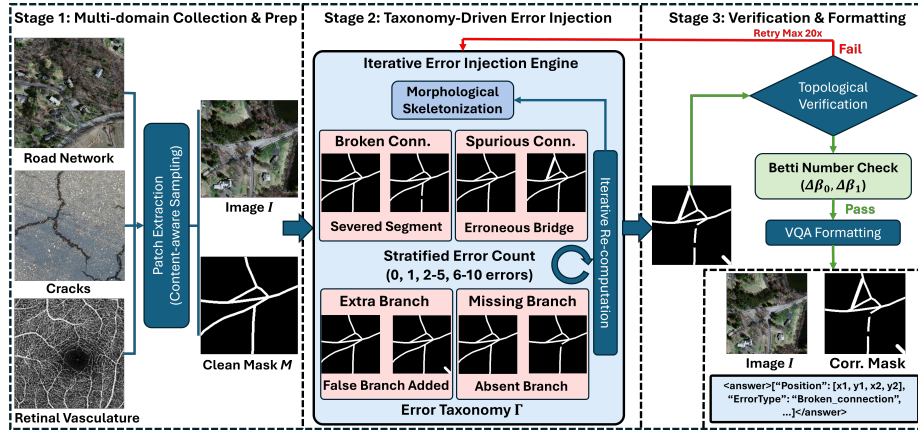


Fig. 3: Overview of the automatic data curation pipeline.

Task Formulation and Error Taxonomy. We formulate topological anomaly detection as a structured prediction problem. Given an input image $I \in \mathbb{R}^{H \times W \times 3}$ and a binary segmentation mask $M \in \{0, 1\}^{H \times W}$, the goal is to produce a set of detections $\mathcal{E} = \{(b_i, t_i)\}_{i=1}^N$, where $b_i = (x_1, y_1, x_2, y_2)$ denotes the bounding box of the i -th error in normalized coordinates and $t_i \in \mathcal{T}$ its type, or $\mathcal{E} = \emptyset$ if no errors exist.

The taxonomy \mathcal{T} is organized along two orthogonal axes: *connectivity* errors that alter the global network graph, and *branching* errors that modify local skeleton structure at endpoints. Within each axis, the two types are complementary, covering both under-segmentation (a missing connection or branch) and over-segmentation (a spurious connection or extra branch). This two-by-two design is exhaustive: every local topological perturbation of a tubular mask falls into exactly one category, and each type is formally verifiable via changes in the Betti numbers (β_0, β_1) , which underpins the automated verification step in our pipeline. The taxonomy \mathcal{T} thus comprises four categories:

- **Broken connection:** a gap severing a continuous segment, increasing β_0 (connected components).
- **Spurious connection:** an erroneous bridge merging distinct segments, decreasing β_0 or increasing β_1 (loops).
- **Missing branch:** a terminal branch absent from the segmentation, reducing branching complexity.
- **Extra branch:** a false branch not present in the ground truth, inflating the branching factor.

Broken and spurious connections alter connectivity directly, whereas missing and extra branches modify the branching structure; both classes significantly affect downstream analyses, such as vessel hierarchy extraction or road network routing.

Multi-Domain Collection. To promote cross-domain generalization, we aggregate data from three data sources: road networks (60%), crack detection (20%),

and retinal vasculature (20%). From each image and its ground-truth mask, we extract 256×256 patches via content-aware sampling, retaining only those in which the foreground covers at least 1% of the area.

Error Injection. For each patch, we inject a controlled number of topological errors into the mask. The error count is sampled from four bins: 0 ($\sim 20\%$, negative samples), 1 ($\sim 20\%$), $2-5$ ($\sim 40\%$), and $6-10$ ($\sim 20\%$), forming a curriculum of increasing complexity. A balanced sampler preferentially selects underrepresented error types. Each injection operates on the morphological skeleton of the current mask, and topological verification serves as a safety fallback. Details will be provided in the Supplementary.

Topological Verification and Formatting. Each injection is verified by computing Betti numbers (β_0, β_1) before and after modification to confirm a genuine topological change; failed injections are retried up to 20 times. Bounding boxes are derived from pixel-wise difference masks, normalized to $[0, 1000]$ and filtered to widths and heights within $[10, 900]$. Each sample pairs the original patch with its (corrupted or clean) segmentation mask and a detection prompt, as shown in Fig. 4; the ground-truth answer is a structured list of error dictionaries in `<answer>` tags sorted in canonical type order (*broken* \rightarrow *spurious* \rightarrow *missing* \rightarrow *extra*) with negative samples returning an empty list. Further details will be provided in the Supplementary.

3.3 Reward Design

The reward function significantly influences detection behavior during RL training. We design a composite reward comprising three terms:

$$R_{\text{total}} = w_{\text{fmt}} \cdot R_{\text{fmt}} + w_{\text{acc}} \cdot R_{\text{acc}} + w_{\text{topo}} \cdot R_{\text{topo}},$$

with $w_{\text{fmt}} = 0.10$, $w_{\text{acc}} = 0.85$, and $w_{\text{topo}} = 0.05$, normalized to sum to unity. The dominant accuracy weight ensures the model prioritizes correct detection, while the format and topological terms provide complementary structural guidance. The *format reward* $R_{\text{fmt}} \in \{0, 1\}$ is a binary gate verifying that the output contains properly delimited answer tags, parses as a valid list of dictionaries with required `Position` and `ErrorType` fields, uses labels from \mathcal{T} , and expresses coordinates as integers in $[0, 1000]$.

Accuracy Reward. The accuracy reward aggregates three complementary sub-objectives:

$$R_{\text{acc}} = R_{\text{det}} + R_{\text{loc}} + R_{\text{type}},$$

covering detection recall/precision, spatial precision, and error-type accuracy, respectively. When both prediction and ground truth are empty (correct negative), $R_{\text{acc}} = 1$; when only one side is empty, $R_{\text{acc}} = 0$.

Type-aware Hungarian Matching. Predictions are assigned to ground-truth errors via optimal bipartite matching within each error type. For a given type $t \in \mathcal{T}$, let \mathcal{G}_t and \mathcal{P}_t denote the subsets of ground-truth and predicted errors of

type t , respectively. We construct an IoU affinity matrix $\mathbf{C}^{(t)} \in \mathbb{R}^{|\mathcal{G}_t| \times |\mathcal{P}_t|}$ with entries $C_{ij}^{(t)} = \text{IoU}(b_i^{\text{gt}}, b_j^{\text{pred}})$ and solve the linear assignment problem:

$$\pi_t^* = \arg \max_{\pi \in \Pi} \sum_{(i,j) \in \pi} C_{ij}^{(t)}, \quad (4)$$

where Π is the set of all valid one-to-one assignments. Pairs with $\text{IoU} < \tau_m$ (we set $\tau_m = 0.1$) are discarded. The union of matched pairs across all types yields the global assignment \mathcal{M} , with unmatched predictions counted as false positives (FP) and unmatched ground-truth errors as false negatives (FN). This procedure guarantees globally optimal, order-independent, one-to-one matching. **Detection Reward (soft F1).** We define a soft F1 score that jointly penalizes false positives and false negatives. Each matched pair $(i, j) \in \mathcal{M}$ contributes a *soft true-positive* score $\phi(\text{IoU}_{ij})$ via a piecewise continuous mapping ϕ (defined below):

$$R_{\text{det}} = \frac{2 \widetilde{\text{TP}}}{2 \widetilde{\text{TP}} + |\text{FP}| + |\text{FN}|}, \quad \widetilde{\text{TP}} = \sum_{(i,j) \in \mathcal{M}} \phi(\text{IoU}_{ij}).$$

This formulation inherently balances precision and recall, and is directly aligned with the F1 metric used at evaluation time.

Localization Reward. To further incentivize precise spatial localization among matched detections, we define

$$R_{\text{loc}} = \frac{1}{|\mathcal{M}|} \sum_{(i,j) \in \mathcal{M}} \phi(\text{IoU}_{ij}), \quad (5)$$

which measures the average localization quality of successfully matched pairs.

Type Bonus. Since the type-aware Hungarian matching exclusively pairs predictions with ground-truth errors of the *same* type, the number of matched pairs directly reflects joint type-localization accuracy. We define the type bonus as the match coverage ratio:

$$R_{\text{type}} = \frac{|\mathcal{M}|}{\max(N_{\text{gt}}, N_{\text{pred}})}, \quad (6)$$

which reaches unity when every error is correctly typed and spatially matched. Here, N_{gt} and N_{pred} denote the number of ground-truth errors and predicted errors from the VLM, respectively. When $|\mathcal{M}| = 0$, we set $R_{\text{loc}} = 0 = R_{\text{topo}} = 0$.

Piecewise Continuous IoU-to-Score Mapping. The function ϕ transforms raw IoU values into reward scores via piecewise power interpolation, ensuring continuous reward values for policy optimization:

$$\phi(\text{IoU}) = \begin{cases} r_1 \cdot (\text{IoU}/\tau_1)^\gamma & \text{if } \text{IoU} < \tau_1 \\ r_{k-1} + (r_k - r_{k-1}) \cdot \left(\frac{\text{IoU} - \tau_{k-1}}{\tau_k - \tau_{k-1}} \right)^\gamma & \text{if } \tau_{k-1} \leq \text{IoU} < \tau_k \\ r_K & \text{if } \text{IoU} \geq \tau_K \end{cases} \quad (7)$$

with thresholds $\{\tau_k\} = \{0.3, 0.5, 0.7, 0.9\}$, rewards $\{r_k\} = \{0.25, 0.55, 0.80, 1.0\}$, smoothness exponent $\gamma = 1.5$, and $k = 2, \dots, K$, providing dense reward signals across localization quality tiers.

Type-Aware Topological Reward. IoU alone does not capture whether a detected region contains topologically significant content. We therefore introduce a reward based on centerline-Dice (clDice) [76], which quantifies structural similarity through skeleton overlap.

For a matched pair (i, j) , let M_i^{gt} and M_j^{corr} denote the ground-truth and corrupted masks cropped to the region of the i -th ground-truth error and j -th predicted error, respectively, with skeletons $S_i^{\text{gt}} = \text{skel}(M_i^{\text{gt}})$ and $S_j^{\text{corr}} = \text{skel}(M_j^{\text{corr}})$. Topological precision and sensitivity are:

$$\text{TPrec}(S_j^{\text{corr}}, M_i^{\text{gt}}) = \frac{|S_j^{\text{corr}} \cap M_i^{\text{gt}}|}{|S_j^{\text{corr}}|}, \quad \text{TSens}(S_i^{\text{gt}}, M_j^{\text{corr}}) = \frac{|S_i^{\text{gt}} \cap M_j^{\text{corr}}|}{|S_i^{\text{gt}}|}, \quad (8)$$

and the clDice score is their harmonic mean:

$$\text{clDice}(M_i^{\text{gt}}, M_j^{\text{corr}}) = 2 \cdot \frac{\text{TPrec} \cdot \text{TSens}}{\text{TPrec} + \text{TSens}}. \quad (9)$$

Regions containing topological errors exhibit low clDice between corrupted and ground-truth masks. The per-box topological reward is defined as $(1 - \text{clDice})$, maximized when centerlines diverge. Crucially, this reward is computed exclusively for Hungarian-matched pairs, inheriting the type-awareness of the matching stage: only predictions that are both correctly typed *and* spatially overlapping with a ground-truth error receive topological credit. For each matched pair $(i, j) \in \mathcal{M}$:

$$R_{\text{topo}}(i, j) = (1 - \text{clDice}(M_i^{\text{gt}}, M_j^{\text{corr}})) \cdot \text{LocPen}(b_j^{\text{pred}}), \quad (10)$$

where b_j^{pred} is the predicted bounding box; unmatched predictions contribute zero. The aggregate topological reward averages over the matched set:

$$R_{\text{topo}} = \frac{1}{|\mathcal{M}|} \sum_{(i,j) \in \mathcal{M}} R_{\text{topo}}(i, j). \quad (11)$$

A localization penalty discourages oversized bounding boxes that trivially capture topological changes:

$$\text{LocPen}(b) = \begin{cases} 1 & \text{if } |b|/|I| \leq \tau_{\text{size}} \\ \max(0, 1 - \lambda \cdot \frac{|b|/|I| - \tau_{\text{size}}}{1 - \tau_{\text{size}}}) & \text{otherwise} \end{cases} \quad (12)$$

with $\tau_{\text{size}} = 0.3$ and $\lambda = 0.8$, applying a steep penalty once a box exceeds 30% of the image area.

4 Experiments

4.1 Experimental Setup

Datasets. To promote cross-domain generalization, we aggregate data from three public sources spanning aerial road networks [57], surface cracks [52], and retinal vasculature [45]. From each source we extract 256×256 patches via content-aware sampling, then inject four types of topological defects (broken/spurious connections, missing/extra branches) through the automated pipeline of Sec. 3.2, with Betti-number verification ensuring genuine topological change. Error counts are stratified into four complexity levels to create a curriculum of increasing difficulty. After quality control, the final dataset comprises 12,900 samples for supervised fine-tuning, 50,300 for reinforcement learning, and a test set of 4,246 samples. All bounding-box coordinates are normalized to $[0, 1000]$ for scale invariance. Full per-source statistics and filtering criteria are in the Supplementary. Both training data and the benchmark will be publicly released.

Evaluation Metrics. We cast evaluation as both a detection and classification task [46]: the model must localize each topological error and identify its type. Predictions are matched to ground-truth errors via type-aware Hungarian matching [35]: a true positive requires both correct type and $\text{IoU} \geq \tau$. We report micro-averaged Precision, Recall, and F1 at $\tau \in \{0.3, 0.5, 0.75\}$, aF1 (COCO-style average over $\tau \in [0.50:0.05:0.95]$), and Macro F1@0.5 for balanced per-type evaluation. Full details are in the Supplementary.

Implementation Details. Details will be provided in the Supplementary.

Base Models. We instantiate Topo-R1 on four open-source models: InternVL-2.5-2B [11], Qwen2.5-VL-3B-Instruct [4], and Qwen3-VL-4B/8B-Instruct [84], following a two-stage pipeline: full-parameter SFT on $\sim 12,900$ labeled samples, then GRPO reinforcement learning on $\sim 50,300$ skeleton-augmented samples using the SFT checkpoint to initialize both π_θ and π_{ref} . We report zero-shot, SFT-only, and Topo-R1 results for each backbone to isolate per-stage gains, and additionally benchmark four closed-source models: GPT-4o [29], GPT-5.2 [77], Gemini-2.5-Flash [14], and Qwen3.5-Plus [65] under identical evaluations.

4.2 Experimental Results

Qualitative Results. As shown in Fig. 4, Topo-R1 accurately detects and classifies topological errors spanning both Betti-number dimensions. For β_0 -level errors, which alter the number of connected components, the model correctly localizes broken connections that sever continuous tubular segments and spurious connections that erroneously merge disjoint structures. For β_1 -level errors, which introduce or eliminate loops in the network graph, Topo-R1 identifies spurious bridges that create closed cycles. In contrast, the SFT baseline consistently returns empty predictions, confirming that topology-aware reinforcement learning is essential to bridge the perception gap.

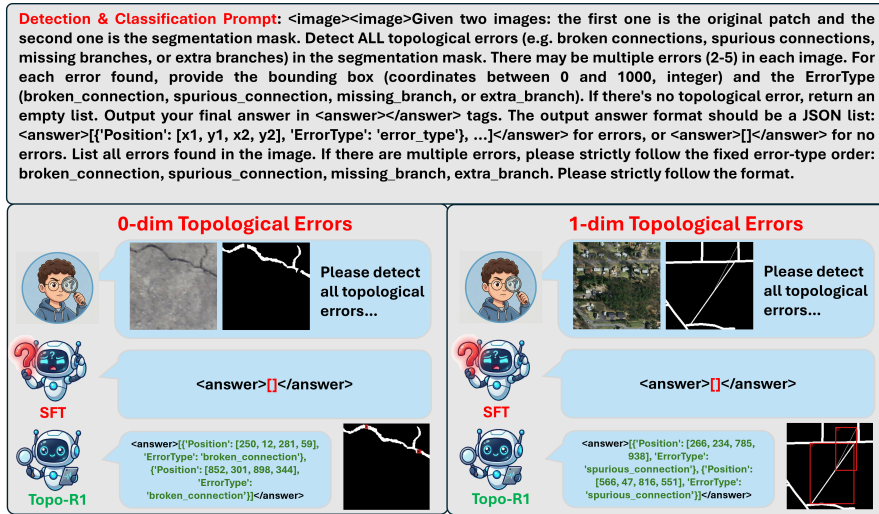


Fig. 4: Qualitative results of topological anomaly detection on 0- and 1-topological errors. **Topo-R1** demonstrates superior capability in the localization and classification of diverse topological errors.

Table 1: Few-shot evaluation (1, 3, and 5 in-context examples). We report detection precision (P), recall (R), and F1 at IoU thresholds 0.3, 0.5, and 0.75, along with the COCO-style average F1 (aF1, IoU 0.5:0.95). “ZS” denotes zero-shot inference. Both zero-shot and few-shot results are almost random, confirming that in-context learning alone cannot elicit topology-aware perception.

Model	Setting	@IoU=0.3			@IoU=0.5			@IoU=0.75			aF1
		P	R	F1	P	R	F1	P	R	F1	
Qwen2.5-VL-3B	ZS	0.0	0.0	0.0	0.0	0.0	0.0	0.0	0.0	0.0	0.0
	1-shot	0.7	0.1	0.1	0.3	0.0	0.0	0.0	0.0	0.0	0.0
	3-shot	0.5	0.0	0.0	0.0	0.0	0.0	0.0	0.0	0.0	0.0
	5-shot	2.3	0.2	0.3	0.4	0.0	0.1	0.0	0.0	0.0	0.0
Qwen3-VL-4B	ZS	0.1	0.1	0.1	0.0	0.0	0.0	0.0	0.0	0.0	0.0
	1-shot	1.4	1.2	1.3	0.5	0.4	0.5	0.1	0.0	0.0	0.1
	3-shot	0.7	0.7	0.7	0.2	0.1	0.2	0.0	0.0	0.0	0.0
	5-shot	1.0	0.9	0.9	0.3	0.3	0.3	0.0	0.0	0.0	0.1
Qwen3-VL-8B	ZS	0.0	0.0	0.0	0.0	0.0	0.0	0.0	0.0	0.0	0.0
	1-shot	1.0	0.2	0.3	0.4	0.1	0.1	0.0	0.0	0.0	0.0
	3-shot	0.2	0.2	0.2	0.1	0.1	0.1	0.0	0.0	0.0	0.0
	5-shot	0.9	0.5	0.6	0.3	0.2	0.2	0.0	0.0	0.0	0.1

Few-Shot Evaluations. Tab. 1 shows that in-context learning cannot elicit topology-aware detection: performance remains near zero across all models and shot counts, with the best result reaching only 0.5% F1@0.5. These results establish that explicit fine-tuning with topology-aware supervision is the necessary pathway to topology-aware detection.

Main Quantitative Results. Tab. 2 reveals three consistent patterns. First, zero-shot performance is uniformly negligible: even the strongest closed-source model achieves only 1.5% F1@0.5 (and 3.2% F1@0.3). Second, SFT provides a necessary foundation by teaching the taxonomy of anomalies and basic localiza-

Table 2: Main results on topological anomaly detection. Same metrics as Tab. 1. Closed-source models are evaluated in a zero-shot setting. “ZS” denotes zero-shot inference, “SFT” denotes supervised fine-tuning, and “Topo-R1” denotes our topology-aware reinforcement fine-tuning. **Bold** indicates the best result in each block.

Model	Method	@IoU=0.3			@IoU=0.5			@IoU=0.75			aF1
		P	R	F1	P	R	F1	P	R	F1	
<i>Closed-Source Models (Zero-Shot)</i>											
GPT-4o	ZS	0.6	0.3	0.4	0.3	0.1	0.1	0.0	0.0	0.0	0.0
GPT-5.2	ZS	2.4	1.7	2.0	1.0	0.7	0.8	0.2	0.1	0.1	0.3
Gemini-2.5-Flash	ZS	3.0	2.4	2.7	1.0	0.9	0.9	0.1	0.1	0.1	0.3
Qwen3.5-Plus	ZS	3.1	3.2	3.2	1.4	1.5	1.5	0.2	0.2	0.2	0.5
<i>Open-Source Models</i>											
InternVL-2.5-2B	ZS	0.0	0.0	0.0	0.0	0.0	0.0	0.0	0.0	0.0	0.0
	SFT	15.9	16.6	16.3	8.8	9.2	9.0	3.2	3.3	3.2	4.0
	Topo-R1	47.3	37.8	42.0	39.2	27.0	32.0	19.2	12.8	15.3	17.1
Qwen2.5-VL-3B	ZS	0.0	0.0	0.0	0.0	0.0	0.0	0.0	0.0	0.0	0.0
	SFT	20.9	16.4	18.4	13.6	10.7	11.9	4.7	3.7	4.1	5.3
	Topo-R1	66.8	50.9	57.8	49.7	37.9	43.0	21.3	16.2	18.4	21.4
Qwen3-VL-4B	ZS	0.1	0.1	0.1	0.0	0.0	0.0	0.0	0.0	0.0	0.0
	SFT	42.6	25.5	31.9	30.7	18.3	23.0	16.2	9.7	12.1	12.8
	Topo-R1	70.0	49.9	58.3	54.3	38.7	45.2	27.0	19.3	22.5	24.7
Qwen3-VL-8B	ZS	0.0	0.0	0.0	0.0	0.0	0.0	0.0	0.0	0.0	0.0
	SFT	38.4	20.5	26.7	29.0	15.5	20.2	16.9	9.0	11.8	11.8
	Topo-R1	69.1	48.5	57.0	53.1	37.3	43.9	27.1	19.0	22.4	24.3

Table 3: The results on the sample-level. Count Acc/MAE measures error counting ability (% and mean absolute error). mPS-F1@0.5: mean per-sample F1 at IoU \geq 0.5 (%), capturing partial credit.

Model	Method	Count Acc \uparrow	Count MAE \downarrow	mPS-F1@0.5 \uparrow
<i>Closed-Source Models (Zero-Shot)</i>				
GPT-4o	ZS	26.3	2.28	10.3
GPT-5.2	ZS	20.3	2.24	8.6
Gemini-2.5-Flash	ZS	22.0	2.35	10.5
Qwen3.5-Plus	ZS	15.5	2.27	5.2
<i>Open-Source Models</i>				
InternVL-2.5-2B	ZS	21.0	3.10	20.4
	SFT	42.8	1.65	21.9
	Topo-R1	46.8	1.28	44.2
Qwen2.5-VL-3B	ZS	13.7	3.23	13.4
	SFT	50.2	1.09	27.3
	Topo-R1	51.5	1.04	56.2
Qwen3-VL-4B	ZS	17.2	2.49	0.9
	SFT	42.0	1.55	37.7
	Topo-R1	54.2	1.02	58.5
Qwen3-VL-8B	ZS	20.4	3.18	20.4
	SFT	41.5	1.64	35.7
	Topo-R1	54.9	1.06	57.5

tion. Third, RL with our composite reward yields consistent improvements over SFT across all backbones, with gains particularly pronounced in precision, indicating that the model learns to produce more accurate detections. Notably, even the smallest **Topo-R1** backbone surpasses all closed-source models by an order

Table 4: Ablation on raw IoU vs. non-linear tiered reward. All metrics in %; **bold**: best per backbone.

Backbone	Reward	F1@.3	F1@.5	F1@.75	aF1	mPS-F1@.5	Cnt.Acc
Qwen2.5-VL-3B	Raw IoU	22.4	14.9	5.6	6.9	29.9	50.1
	Topo-R1	57.8	43.0	18.4	21.4	56.2	51.5
Qwen3-VL-8B	Raw IoU	29.7	22.3	12.3	12.6	37.5	43.5
	Topo-R1	57.0	43.9	22.4	24.3	57.5	54.9

Table 5: Ablation on IoU threshold set (Qwen3-VL-4B). **Linear**: piecewise linear interpolation between tier boundaries; **COCO**: thresholds {0.5, 0.75, 0.9}. All metrics in %; **bold**: best per column.

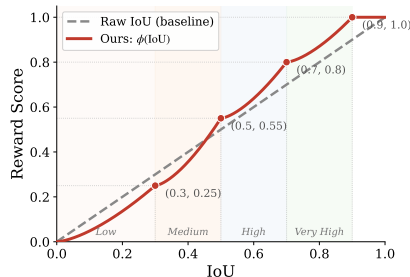
Method	F1@.3	F1@.5	F1@.75	aF1	mPS-F1@.5	Cnt.Acc
SFT	31.9	23.0	12.1	12.8	37.7	42.0
Linear	56.8	43.0	20.7	23.2	57.1	54.9
COCO	57.2	43.5	21.7	23.9	57.5	54.1
Topo-R1	58.3	45.2	22.5	24.7	58.5	54.2

of magnitude, and the best result of 45.2% F1@0.5 on Qwen3-VL-4B confirms that topology-aware supervision, rather than model scale, is the decisive factor.

4.3 Ablation Studies

Ablation on Raw IoU Reward. We compare our non-linear tiered mapping ϕ against a raw IoU baseline that directly uses the IoU value as the reward score without any piecewise mapping ($\phi(\text{IoU}) = \text{IoU}$). The reward design comparisons are shown in Fig. 5. As shown in Tab. 4, the raw IoU reward underperforms our design by roughly 27–35 points at F1@0.3 and over 15 points at F1@0.5 across both backbones, confirming that a flat, unshaped reward signal fails to incentivize the precise localization needed for high-IoU detections.

Ablation on Threshold Selection. As shown in Tab. 5, our piecewise non-linear reward is more robust than alternative threshold designs. Compared with Linear (thresholds {0.3, 0.5, 0.7, 0.9}) and COCO (thresholds {0.5, 0.75, 0.9}), our design achieves the best F1 across all IoU levels, as the non-linear mapping ϕ provides sharper reward shaping at critical IoU boundaries. Because IoU itself changes non-linearly during training, a linear mapping introduces noisy and inconsistent reward signals, whereas our piecewise non-linear design absorbs this variability within each tier, yielding more stable optimization and stronger overall performance.

**Fig. 5:** IoU-to-score mapping ϕ for different reward designs.

5 Conclusion

We introduced **Topo-R1**, the first vision-language framework for detecting and classifying topological anomalies in tubular structures. We built an automated pipeline that injects four controlled topological anomalies with topological verification, trained a VLM via SFT, then GRPO, with a composite reward that combines format consistency, decoupled detection accuracy with type-aware Hungarian matching, and a type-conditioned cDice term. **Topo-R1** substantially outperforms all baseline VLMs across multiple detection metrics and generalizes across domains, demonstrating that topology-aware reward shaping enables fine-grained structural understanding in vision-language models.

References

1. Alayrac, J.B., Donahue, J., Luc, P., Miech, A., Barr, I., Hasson, Y., Lenc, K., Mensch, A., Millican, K., Reynolds, M., et al.: Flamingo: A visual language model for few-shot learning. In: *NeurIPS* (2022)
2. Azar, M.G., Rowland, M., Piot, B., Guo, D., Calandriello, D., Valko, M., Munos, R.: A general theoretical paradigm to understand learning from human feedback. In: *AISTATS* (2024)
3. Bai, J., Bai, S., Yang, S., Wang, S., Tan, S., Wang, P., Lin, J., Zhou, C., Zhou, J.: Qwen-vl: A versatile vision-language model for understanding, localization, text reading, and beyond. *arXiv preprint arXiv:2308.12966* (2023)
4. Bai, S., Chen, K., Liu, X., Wang, J., Ge, W., Song, S., Dang, K., Wang, P., Wang, S., Tang, J., et al.: Qwen2. 5-vl technical report. *arXiv preprint arXiv:2502.13923* (2025)
5. Batra, H., Tu, H., Chen, H., Lin, Y., Xie, C., Clark, R.: Spatialthinker: Reinforcing 3d reasoning in multimodal llms via spatial rewards. In: *NeurIPS Workshop on Space in Vision, Language, and Embodied AI* (2025)
6. BenTaieb, A., Hamarneh, G.: Topology aware fully convolutional networks for histology gland segmentation. In: *MICCAI* (2016)
7. Brown, J., Kirjner, A., Vivekananthan, A., Boyden, E.: Connectomebench: Can llms proofread the connectome? *arXiv preprint arXiv:2511.05542* (2025)
8. Chao, Y., Liu, J., Tang, J., Wu, G.: Anomalyr1: A grpo-based end-to-end mllm for industrial anomaly detection. *arXiv preprint arXiv:2504.11914* (2025)
9. Chen, K., Zhang, Z., Zeng, W., Zhang, R., Zhu, F., Zhao, R.: Shikra: Unleashing multimodal llm’s referential dialogue magic. *arXiv preprint arXiv:2306.15195* (2023)
10. Chen, Z., Wang, W., Tian, H., Ye, S., Gao, Z., Cui, E., Tong, W., Hu, K., Luo, J., Ma, Z., et al.: How far are we to gpt-4v? closing the gap to commercial multimodal models with open-source suites. *Science China Information Sciences* (2024)
11. Chen, Z., Wu, J., Wang, W., Su, W., Chen, G., Xing, S., Zhong, M., Zhang, Q., Zhu, X., Lu, L., Li, B., Luo, P., Lu, T., Qiao, Y., Dai, J.: Internvl: Scaling up vision foundation models and aligning for generic visual-linguistic tasks. In: *CVPR* (2024)
12. Christiano, P.F., Leike, J., Brown, T., Marber, M., Legg, S., Amodei, D.: Deep reinforcement learning from human preferences. In: *NeurIPS* (2017)
13. Clough, J.R., Byrne, N., Oksuz, I., Zimmer, V.A., Schnabel, J.A., King, A.P.: A topological loss function for deep-learning based image segmentation using persistent homology. *TPAMI* (2020)
14. Comanici, G., Bieber, E., Schaekermann, M., Pasupat, I., Sachdeva, N., Dhillon, I., Blistein, M., Ram, O., Zhang, D., Rosen, E., et al.: Gemini 2.5: Pushing the frontier with advanced reasoning, multimodality, long context, and next generation agentic capabilities. *arXiv preprint arXiv:2507.06261* (2025)
15. Dai, W., Li, J., Li, D., Tiong, A.M.H., Zhao, J., Wang, W., Li, B., Fung, P., Hoi, S.: Instructblip: Towards general-purpose vision-language models with instruction tuning. In: *NeurIPS* (2023)
16. Decroocq, M., Poon, C., Schlachter, M., Skibbe, H.: Benchmarking evaluation metrics for tubular structure segmentation in biomedical images. In: *International Workshop on Shape in Medical Imaging* (2025)
17. Deitke, M., Clark, C., Lee, S., Tripathi, R., Yang, Y., Park, J.S., Salehi, M., Muennighoff, N., Lo, K., Soldaini, L., et al.: Molmo and pixmo: Open weights and open data for state-of-the-art vision-language models. In: *CVPR* (2025)

18. Edelsbrunner, H., Harer, J.: Computational topology: an introduction. American Mathematical Soc. (2010)
19. Ethayarajh, K., Xu, W., Muennighoff, N., Jurafsky, D., Kiela, D.: Kto: Model alignment as prospect theoretic optimization. In: ICML (2024)
20. Fan, Y., He, X., Yang, D., Zheng, K., Kuo, C.C., Zheng, Y., Guan, X., Wang, X.E.: Grit: Teaching mllms to think with images. In: NeurIPS (2025)
21. Feng, K., Gong, K., Li, B., Guo, Z., Wang, Y., Peng, T., Wu, J., Zhang, X., Wang, B., Yue, X.: Video-r1: Reinforcing video reasoning in mllms. In: NeurIPS (2025)
22. Frangi, A.F., Niessen, W.J., Vincken, K.L., Viergever, M.A.: Multiscale vessel enhancement filtering. In: MICCAI (1998)
23. Gemini Team, Google DeepMind: Gemini: A family of highly capable multimodal models. arXiv preprint arXiv:2312.11805 (2023)
24. Gu, Z., Zhu, B., Zhu, G., Chen, Y., Tang, M., Wang, J.: Anomalygpt: Detecting industrial anomalies using large vision-language models. In: AAAI (2024)
25. Hu, X.: Structure-aware image segmentation with homotopy warping. In: NeurIPS (2022)
26. Hu, X., Li, F., Samaras, D., Chen, C.: Topology-preserving deep image segmentation. In: NeurIPS (2019)
27. Huang, Q., Dai, W., Liu, J., He, W., Jiang, H., Song, M., Chen, J., Yao, C., Song, J.: Boosting mllm reasoning with text-debiased hint-grpo. In: ICCV (2025)
28. Huang, W., Jia, B., Zhai, Z., Cao, S., Ye, Z., Zhao, F., Xu, Z., Hu, Y., Lin, S.: Vision-r1: Incentivizing reasoning capability in multimodal large language models. In: ICLR (2026)
29. Hurst, A., Lerer, A., Goucher, A.P., Perelman, A., Ramesh, A., Clark, A., Ostrow, A., Welihinda, A., Hayes, A., Radford, A., et al.: Gpt-4o system card. arXiv preprint arXiv:2410.21276 (2024)
30. Isensee, F., Jaeger, P.F., Kohl, S.A.A., Petersen, J., Maier-Hein, K.H.: nnu-net: A self-configuring method for deep learning-based biomedical image segmentation. Nature Methods (2021)
31. Jiang, X., Li, J., Deng, H., Liu, Y., Gao, B.B., Zhou, Y., Li, J., Wang, C., Zheng, F.: Mmad: A comprehensive benchmark for multimodal large language models in industrial anomaly detection. In: ICLR (2025)
32. Karamcheti, S., Nair, S., Balakrishna, A., Liang, P., Kollar, T., Sadigh, D.: Prismatic vlms: Investigating the design space of visually-conditioned language models. In: ICML (2024)
33. Khandouzi, A., Ariafar, A., Mashayekhpour, Z., Pazira, M., Baleghi, Y.: Retinal vessel segmentation, a review of classic and deep methods. Annals of Biomedical Engineering (2022)
34. Kirchhoff, Y., Rokuss, M.R., Roy, S., Kovacs, B., Ulrich, C., Wald, T., Zenk, M., Vollmuth, P., Kleesiek, J., Isensee, F., et al.: Skeleton recall loss for connectivity conserving and resource efficient segmentation of thin tubular structures. In: ECCV (2024)
35. Kuhn, H.W.: The hungarian method for the assignment problem. Naval Research Logistics Quarterly (1955)
36. Lai, X., Tian, Z., Chen, Y., Li, Y., Yuan, Y., Liu, S., Jia, J.: Lisa: Reasoning segmentation via large language model. In: CVPR (2024)
37. Lai, Y., Zhong, J., Li, M., Zhao, S., Li, Y., Psounis, K., Yang, X.: Med-r1: Reinforcement learning for generalizable medical reasoning in vision-language models. TMI (2026)
38. Lee, Y.: Qwen2-vl-finetune (2024)

39. Li, C., Wong, C., Zhang, S., Usuyama, N., Liu, H., Yang, J., Naumann, T., Poon, H., Gao, J.: Llava-med: Training a large language and vision assistant for biomedicine in one day. In: *NeurIPS* (2023)
40. Li, J., Li, D., Savarese, S., Hoi, S.: Blip-2: Bootstrapping language-image pre-training with frozen image encoders and large language models. In: *ICML* (2023)
41. Li, L., Zhao, Z., Wang, R., Poria, S., Bing, L.: Silkie: Preference distillation for large visual language models. *arXiv preprint arXiv:2312.10665* (2024)
42. Li, L., Ma, Q., Ouyang, C., Li, Z., Meng, Q., Zhang, W., Qiao, M., Kyriakopoulou, V., Hajnal, J.V., Rueckert, D., et al.: Robust segmentation via topology violation detection and feature synthesis. In: *MICCAI* (2023)
43. Li, L., Ma, Q., Ouyang, C., Paetzold, J.C., Rueckert, D., Kainz, B.: Topology optimization in medical image segmentation with fast χ euler characteristic. *TMI* (2025)
44. Li, L., Wang, H., Baugh, M., Ma, Q., Zhang, W., Ouyang, C., Rueckert, D., Kainz, B.: Universal topology refinement for medical image segmentation with polynomial feature synthesis. In: *MICCAI* (2024)
45. Li, M., Chen, Y., Ji, Z., Xie, K., Yuan, S., Chen, Q., Li, S.: Image projection network: 3d to 2d image segmentation in octa images. *TMI* (2020)
46. Lin, T.Y., Maire, M., Belongie, S., Hays, J., Perona, P., Ramanan, D., Dollár, P., Zitnick, C.L.: Microsoft coco: Common objects in context. In: *ECCV* (2014)
47. Liu, H., Li, C., Li, Y., Lee, Y.J.: Improved baselines with visual instruction tuning. In: *CVPR* (2024)
48. Liu, H., Li, C., Wu, Q., Lee, Y.J.: Visual instruction tuning. In: *NeurIPS* (2023)
49. Liu, S., Zeng, Z., Ren, T., Li, F., Zhang, H., Yang, J., Jiang, Q., Li, C., Yang, J., Su, H., et al.: Grounding dino: Marrying dino with grounded pre-training for open-set object detection. In: *ECCV* (2024)
50. Liu, W., Li, A., Wu, Z., Li, Y., Ge, B., Lan, G., Chen, S., Li, M., Liu, Y., Yuan, X., Dong, N.: Revealing hierarchical structure of leaf venations in plant science via label-efficient segmentation: Dataset and method. In: *IJCAI* (2024)
51. Liu, X., Tan, H., Wang, W., Chen, Z.: Deep learning based retinal vessel segmentation and hypertensive retinopathy quantification using heterogeneous features cross-attention neural network. *Frontiers in Medicine* (2024)
52. Liu, Y., Yao, J., Lu, X., Xie, R., Li, L.: Deepcrack: A deep hierarchical feature learning architecture for crack segmentation. *Neurocomputing* (2019)
53. Liu, Y., Peng, B., Zhong, Z., Yue, Z., Lu, F., Yu, B., Jia, J.: Seg-zero: Reasoning-chain guided segmentation via cognitive reinforcement. *arXiv preprint arXiv:2503.06520* (2025)
54. Liu, Y., Qu, T., Zhong, Z., Peng, B., Liu, S., Yu, B., Jia, J.: Visionreasoner: Unified reasoning-integrated visual perception via reinforcement learning. In: *ICLR* (2026)
55. Liu, Z., Sun, Z., Zang, Y., Dong, X., Cao, Y., Duan, H., Lin, D., Wang, J.: Visual-rlft: Visual reinforcement fine-tuning. In: *ICCV* (2025)
56. Lux, L., Berger, A.H., Weers, A., Stucki, N., Rueckert, D., Bauer, U., Paetzold, J.C.: Topograph: An efficient graph-based framework for strictly topology preserving image segmentation. *arXiv preprint arXiv:2411.03228* (2024)
57. Mnih, V.: *Machine Learning for Aerial Image Labeling*. Ph.D. thesis, University of Toronto (2013)
58. Moor, M., Huang, Q., Wu, S., Yasunaga, M., Dalmia, Y., Leskovec, J., Zakka, C., Reis, E.P., Rajpurkar, P.: Med-flamingo: a multimodal medical few-shot learner. In: *Machine learning for health (ML4H)* (2023)

59. Mosinska, A., Marquez-Neila, P., Koziński, M., Fua, P.: Beyond the pixel-wise loss for topology-aware delineation. In: CVPR (2018)
60. Mou, L., Zhao, Y., Fu, H., Liu, Y., Cheng, J., Zheng, Y., Su, P., Yang, J., Chen, L., Frangi, A.F., et al.: Cs²-net: Deep learning segmentation of curvilinear structures in medical imaging. MedIA (2021)
61. OpenAI: Gpt-4v(ision) system card. OpenAI Technical Report (2023)
62. Ouyang, L., Wu, J., Jiang, X., Almeida, D., Wainwright, C.L., Mishkin, P., Zhang, C., Agarwal, S., Slama, K., Ray, A., et al.: Training language models to follow instructions with human feedback. In: NeurIPS (2022)
63. Pan, J., Liu, C., Wu, J., Liu, F., Zhu, J., Li, H.B., Chen, C., Ouyang, C., Rueckert, D.: Medvlm-r1: Incentivizing medical reasoning capability of vision-language models (vlms) via reinforcement learning. In: MICCAI (2025)
64. Peng, Z., Wang, W., Dong, L., Hao, Y., Huang, S., Ma, S., Wei, F.: Kosmos-2: Grounding multimodal large language models to the world. In: ICLR (2024)
65. Qwen Team: Qwen3.5: Towards native multimodal agents (February 2026)
66. Radford, A., Kim, J.W., Hallacy, C., Ramesh, A., Goh, G., Agarwal, S., Sastry, G., Askell, A., Mishkin, P., Clark, J., et al.: Learning transferable visual models from natural language supervision. In: ICML (2021)
67. Rafailov, R., Sharma, A., Mitchell, E., Ermon, S., Manning, C.D., Finn, C.: Direct preference optimization: Your language model is secretly a reward model. In: NeurIPS (2023)
68. Rasley, J., Rajbhandari, S., Ruwase, O., He, Y.: Deepspeed: System optimizations enable training deep learning models with over 100 billion parameters. In: KDD (2020)
69. Ronneberger, O., Fischer, P., Brox, T.: U-net: Convolutional networks for biomedical image segmentation. In: MICCAI (2015)
70. Sarch, G.H., Saha, S., Khandelwal, N., Jain, A., Tarr, M.J., Kumar, A., Fragkiadaki, K.: Grounded reinforcement learning for visual reasoning. In: NeurIPS (2025)
71. Schulman, J., Wolski, F., Dhariwal, P., Radford, A., Klimov, O.: Proximal policy optimization algorithms. arXiv preprint arXiv:1707.06347 (2017)
72. Shao, Z., Wang, P., Zhu, Q., Xu, R., Song, J., Bi, X., Zhang, H., Zhang, M., Li, Y., Wu, Y., et al.: Deepseekmath: Pushing the limits of mathematical reasoning in open language models. arXiv preprint arXiv:2402.03300 (2024)
73. Shen, C., Wei, W., Qu, X., Cheng, Y.: Satori-r1: Incentivizing multimodal reasoning with spatial grounding and verifiable rewards. arXiv preprint arXiv:2505.19094 (2025)
74. Shen, H., Liu, P., Li, J., Fang, C., Ma, Y., Liao, J., Shen, Q., Zhang, Z., Zhao, K., Zhang, Q., et al.: Vlm-r1: A stable and generalizable r1-style large vision-language model. arXiv preprint arXiv:2504.07615 (2025)
75. Sheng, G., Zhang, C., Ye, Z., Wu, X., Zhang, W., Zhang, R., Peng, Y., Lin, H., Wu, C.: Hybridflow: A flexible and efficient rlhf framework. arXiv preprint arXiv:2409.19256 (2024)
76. Shit, S., Paetzold, J.C., Sekuboyina, A., Ezhov, I., Unger, A., Zhylka, A., Plum, J.P., Bauer, U., Menze, B.H.: cldice-a novel topology-preserving loss function for tubular structure segmentation. In: CVPR (2021)
77. Singh, A., Fry, A., Perelman, A., Tart, A., Ganesh, A., El-Kishky, A., McLaughlin, A., Low, A., Ostrow, A., Ananthram, A., et al.: Openai gpt-5 system card. arXiv preprint arXiv:2601.03267 (2025)
78. Staal, J., Abramoff, M.D., Niemeijer, M., Viergever, M.A., Ginneken, B.V.: Ridge-based vessel segmentation in color images of the retina. TMI (2004)

79. Stucki, N., Bürgin, V., Paetzold, J.C., Bauer, U.: Efficient betti matching enables topology-aware 3d segmentation via persistent homology. arXiv preprint arXiv:2407.04683 (2024)
80. Stucki, N., Paetzold, J.C., Shit, S., Menze, B., Bauer, U.: Topologically faithful image segmentation via induced matching of persistence barcodes. In: ICML (2023)
81. Su, Y., Li, T., Liu, J., Ma, C., Ning, J., Tang, C., Ju, S., Ye, J., Chen, P., Hu, M., et al.: Gmai-vl-r1: Harnessing reinforcement learning for multimodal medical reasoning. arXiv preprint arXiv:2504.01886 (2025)
82. Sun, Z., Shen, S., Cao, S., Liu, H., Li, C., Shen, Y., Gan, C., Gui, L.Y., Wang, Y.X., Yang, Y., et al.: Aligning large multimodal models with factually augmented rlhf. In: ACL (2024)
83. Tan, H., Ji, Y., Hao, X., Chen, X., Wang, P., Wang, Z., Zhang, S.: Reason-rft: Reinforcement fine-tuning for visual reasoning. In: NeurIPS (2025)
84. Team, Q.: Qwen3 technical report (2025), <https://arxiv.org/abs/2505.09388>
85. Tong, P., Brown, E., Wu, P., Woo, S., Iyer, A.J.V., Akula, S.C., Yang, S., Yang, J., Middepogu, M., Wang, Z., et al.: Cambrian-1: A fully open, vision-centric exploration of multimodal llms. In: NeurIPS (2024)
86. Wang, F., Zhou, W., Huang, J.Y., Xu, N., Zhang, S., Poon, H., Chen, M.: mdpo: Conditional preference optimization for multimodal large language models. In: EMNLP (2024)
87. Wang, H., Qu, C., Huang, Z., Chu, W., Lin, F., Chen, W.: Vl-rethinker: Incentivizing self-reflection of vision-language models with reinforcement learning. In: NeurIPS (2025)
88. Wang, P., Bai, S., Tan, S., Wang, S., Fan, Z., Bai, J., Chen, K., Liu, X., Wang, J., Ge, W., et al.: Qwen2-vl: Enhancing vision-language model’s perception of the world at any resolution. arXiv preprint arXiv:2409.12191 (2024)
89. Wang, W., Lv, Q., Yu, W., Hong, W., Qi, J., Wang, Y., Ji, J., Yang, Z., Zhao, L., XiXuan, S., et al.: Cogvlm: Visual expert for pretrained language models. In: NeurIPS (2024)
90. Xia, J., Zang, Y., Gao, P., Li, S., Zhou, K.: Visionary-r1: Mitigating shortcuts in visual reasoning with reinforcement learning. arXiv preprint arXiv:2505.14677 (2025)
91. Xu, H., Nie, Y., Wang, H., Chen, Y., Li, W., Ning, J., Liu, L., Wang, H., Zhu, L., Liu, J., et al.: Medground-r1: Advancing medical image grounding via spatial-semantic rewarded group relative policy optimization. In: MICCAI (2025)
92. Xu, J., Lo, S.Y., Safaei, B., Patel, V.M., Dwivedi, I.: Towards zero-shot anomaly detection and reasoning with multimodal large language models. In: CVPR (2025)
93. Xu, M., Hu, X., Abousamra, S., Li, C., Chen, C.: Match: Multi-faceted adaptive topo-consistency for semi-supervised histopathology segmentation. In: NeurIPS (2025)
94. Xu, M., Hu, X., Gupta, S., Abousamra, S., Chen, C.: Semi-supervised segmentation of histopathology images with noise-aware topological consistency. In: ECCV (2024)
95. Yang, Y., He, X., Pan, H., Jiang, X., Deng, Y., Yang, X., Lu, H., Yin, D., Rao, F., Zhu, M., et al.: R1-onevision: Advancing generalized multimodal reasoning through cross-modal formalization. In: ICCV (2025)
96. You, H., Zhang, H., Gan, Z., Du, X., Zhang, B., Wang, Z., Cao, L., Chang, S.F., Yang, Y.: Ferret: Refer and ground anything anywhere at any granularity. In: ICLR (2024)

97. Yu, E., Lin, K., Zhao, L., Wei, Y., Peng, Y., Wei, H., Sun, J., Han, C., Ge, Z., Zhang, X., et al.: Perception-r1: Pioneering perception policy with reinforcement learning. In: NeurIPS (2025)
98. Yu, T., Yao, Y., Zhang, H., He, T., Han, Y., Cui, G., Hu, J., Liu, Z., Zheng, H.T., Sun, M., et al.: Rlhf-v: Towards trustworthy mllms via behavior alignment from fine-grained correctional human feedback. In: CVPR (2024)
99. Yu, T., Zhang, H., Li, Q., Xu, Q., Yao, Y., Chen, D., Lu, X., Cui, G., Dang, Y., He, T., Feng, X., Song, J., Zheng, B., Liu, Z., Chua, T.S., Sun, M.: Rlaif-v: Open-source ai feedback leads to super gpt-4v trustworthiness. In: CVPR (2025)
100. Zhang, J., Huang, J., Yao, H., Liu, S., Zhang, X., Lu, S., Tao, D.: R1-vl: Learning to reason with multimodal large language models via step-wise group relative policy optimization. In: ICCV (2025)
101. Zhang, S., Xu, Y., Usuyama, N., Xu, H., Bagga, J., Tinn, R., Preston, S., Rao, R., Wei, M., Valluri, N., Wong, C., Tupini, A., Wang, Y., Mazzola, M., Shukla, S., Liden, L., Gao, J., Crabtree, A., Piening, B., Bifulco, C., Lungren, M.P., Naumann, T., Wang, S., Poon, H.: A multimodal biomedical foundation model trained from fifteen million image-text pairs. NEJM AI (2024)
102. Zheng, Y., Lu, J., Wang, S., Feng, Z., Kuang, D., Xiong, Y., Zhang, R.: Easyr1: An efficient, scalable, multi-modality rl training framework (2025)
103. Zhou, Z., Rahman Siddiquee, M.M., Tajbakhsh, N., Liang, J.: Unet++: Redesigning skip connections to exploit multiscale features in image segmentation. TMI (2020)
104. Zhu, D., Chen, J., Shen, X., Li, X., Elhoseiny, M.: Minigpt-4: Enhancing vision-language understanding with advanced large language models. arXiv preprint arXiv:2304.10592 (2023)
105. Zhu, L., Ouyang, B., Zhang, Y., Cheng, T., Hu, R., Shen, H., Ran, L., Chen, X., Yu, L., Liu, W., et al.: Lens: Learning to segment anything with unified reinforced reasoning. arXiv preprint arXiv:2508.14153 (2025)

Topo-R1: Detecting Topological Anomalies via Vision-Language Models —Supplementary Material—

No Author Given

No Institute Given

6 Evaluation Metrics and Protocol Details

This appendix provides formal definitions of the evaluation protocol and all metrics used in our experiments. The model must produce a set of anomaly detections, each consisting of a bounding box $b = [x_1, y_1, x_2, y_2]$ (normalized to $[0, 1000] \times [0, 1000]$) and a type label $t \in \mathcal{T}$, where

$$\mathcal{T} = \{\text{broken_conn.}, \text{spurious_conn.}, \text{missing_branch}, \text{extra_branch}\}.$$

Let $\{g_i\}_{i=1}^{N_g}$ and $\{p_j\}_{j=1}^{N_p}$ denote the ground-truth and predicted anomalies for a given sample, respectively.

Matching Protocol. All metrics are built upon a type-aware Hungarian matching that pairs predictions with ground-truth annotations. For each anomaly type $t \in \mathcal{T}$, we partition both sets by type (G_t, P_t) , construct an IoU cost matrix $C^{(t)} \in \mathbb{R}^{|G_t| \times |P_t|}$ with $C_{ij}^{(t)} = \text{IoU}(g_i, p_j)$, and solve the optimal linear assignment to maximize total IoU. A match (g_i, p_j) is accepted only if $\text{IoU}(g_i, p_j) \geq \tau$. Because matching is performed separately within each type, a prediction that correctly localizes an anomaly but assigns the wrong type is counted as both an FP and an FN, ensuring that classification correctness is strictly enforced.

Detection Metrics. Our primary metrics evaluate how well the model detects anomalies at varying localization strictness. Micro-averaged precision (P), recall (R), and F1 are computed by summing TP, FP, and FN across all test samples:

$$P = \frac{\text{TP}}{\text{TP} + \text{FP}}, \quad R = \frac{\text{TP}}{\text{TP} + \text{FN}}, \quad F1 = \frac{2PR}{P + R}. \quad (1)$$

We report P, R, and F1 at IoU thresholds $\tau \in \{0.3, 0.5, 0.75\}$ (Tabs. 1 and 2). To summarize performance across thresholds, we compute the COCO-style average F1: $\text{aF1} = \frac{1}{10} \sum_{k=0}^9 F1_{\tau=0.50+0.05k}$, which penalizes models that perform well at lenient thresholds but degrade at stricter ones (Tabs. 1, 2, 4 and 5).

Classification Metrics. To assess type discrimination beyond aggregate detection, we compute per-type F1 by accumulating TP/FP/FN separately for each anomaly type across all samples. Macro F1 is the unweighted average:

$$\text{Macro-F1} = \frac{1}{|\mathcal{T}^+|} \sum_{t \in \mathcal{T}^+} F1_t, \quad \mathcal{T}^+ = \{t : \text{TP}_t + \text{FN}_t > 0\}. \quad (2)$$

This ensures that rare types (*e.g.*, `extra_branch`, 1181 instances) are weighted equally with common types (*e.g.*, `broken_connection`, 4508 instances). Per-type and Macro F1 are reported in Tabs. 7, 9 and 11.

Sample-Level Metrics. While the above metrics aggregate across the full test set, we also report per-sample statistics (Tabs. 3 to 5). *Anomaly Count Accuracy* measures the fraction of samples where the predicted count exactly matches the ground truth: $\frac{1}{N} \sum_{i=1}^N \mathbb{1}[N_{\text{pred}}^{(i)} = N_{\text{gt}}^{(i)}]$. *Anomaly Count MAE* captures the average deviation: $\text{MAE} = \frac{1}{N} \sum_{i=1}^N |N_{\text{gt}}^{(i)} - N_{\text{pred}}^{(i)}|$. *Mean Per-Sample F1 (mPS-F1)* computes F1 per sample using type-aware matching at threshold τ , then averages: $\text{mPS-F1@}\tau = \frac{1}{N} \sum_{i=1}^N F1_{\tau}^{(i)}$. Note that for anomaly-free samples ($N_{\text{gt}} = N_{\text{pred}} = 0$), F1 is defined as 1.0; since 20.4% of test samples have no anomalies, mPS-F1 is systematically higher than micro-averaged F1. *Negative Sample Accuracy* measures the fraction of anomaly-free samples where the model correctly predicts $N_{\text{pred}} = 0$, reflecting the ability to suppress false alarms.

Localization Quality. To measure the spatial precision of correctly detected anomalies, we report the mean IoU among all matched pairs at $\tau = 0.5$:

$$\overline{\text{IoU}} = \frac{1}{|\mathcal{M}|} \sum_{(g,p) \in \mathcal{M}} \text{IoU}(g,p), \quad (3)$$

where \mathcal{M} is the set of accepted matches. This complements F1 by isolating localization accuracy from detection completeness. Different anomaly types exhibit different spatial extents: broken connections are typically small (~ 10 – 30 px), while spurious connections may span ~ 100 – 500 px. For small ground-truth boxes, even minor localization offsets cause IoU to fall below the threshold, partly explaining the consistently higher per-type F1 for spurious connections. We mitigate this by reporting at multiple IoU thresholds, including the lenient $\tau = 0.3$.

7 Implementation Details

In this section, we provide implementation details that complement the reward formulation described in Sec. 3. Training proceeds in two stages: supervised fine-tuning (SFT) followed by reinforcement fine-tuning (RFT).

Supervised Fine-Tuning (SFT). The model is first trained with standard supervised fine-tuning on the curated SFT dataset. We use a global batch size of 16 (2 samples per device across 8 GPUs with 1 gradient accumulation step) and train for 3 epochs. Three separate learning rates are applied: 1×10^{-6} for the language model backbone, 2×10^{-6} for the vision encoder, and 1×10^{-5} for the vision-language merger module. All learning rates follow a cosine decay schedule with a warmup ratio of 0.03. Additional regularization includes weight decay of 0.1 and gradient clipping at a maximum norm of 1.0. Training uses BF16 precision with gradient checkpointing and DeepSpeed ZeRO-2 offloading [68].

Reinforcement Fine-Tuning (RFT). Starting from the SFT checkpoint, we apply GRPO for reinforcement fine-tuning. For each training prompt, the rollout worker generates $n = 4$ candidate responses (the number of generations per prompt), which are scored by the reward function and used to compute group-relative advantages. The rollout batch size is 256 prompts per step, and the global batch size for the actor update is 64 with a per-device micro-batch of 1. Training runs for 10 epochs with a learning rate of 5×10^{-7} , a linear warmup over the first 10% of updates, and weight decay of 10^{-2} . A KL penalty with coefficient 0.05 is applied against the reference policy using the low-variance KL estimator. Rollout sampling uses a temperature of 0.8 and a top- p of 0.95; gradient clipping is set to a maximum norm of 1.0. Model parameters are shared with FSDP (full-shard mode) across 8 GPUs. All models with 4B parameters or fewer are trained on $8 \times$ NVIDIA RTX 6000 Ada Generation GPUs (48 GB each), and Qwen3-VL-8B is trained on $8 \times$ NVIDIA H100 80 GB HBM3 GPUs.

Accuracy Reward. Three corner cases are handled before Hungarian matching: (i) both $N_{\text{gt}} = 0$ and $N_{\text{pred}} = 0$ (true negative) yields $R_{\text{acc}} = 1.0$; (ii) $N_{\text{gt}} = 0$ but $N_{\text{pred}} > 0$ (all false positives) yields $R_{\text{acc}} = 0.0$; (iii) $N_{\text{pred}} = 0$ but $N_{\text{gt}} > 0$ (all false negatives) yields $R_{\text{acc}} = 0.0$. Otherwise, predictions and ground-truth errors are partitioned by type, and for each type $t \in \mathcal{T}$ an IoU cost matrix is constructed and solved via optimal linear assignment. Matched pairs with $\text{IoU}_{ij} < \tau_m = 0.1$ are discarded. Because matching is per-type, type accuracy is implicitly encoded in the assignment.

clDice Reward. For each matched pair $(i, j) \in \mathcal{M}$, we apply *separate* crops to the corrupted and ground-truth masks (and their skeletons) using the predicted and ground-truth bounding boxes, respectively. This design allows clDice to verify whether the predicted region genuinely contains a topological anomaly: if the corrupted crop (localized by the model) exhibits a different centerline topology from the clean ground-truth crop, the resulting low clDice yields a high $(1 - \text{clDice})$ reward, while a false detection produces similar crops and thus a low reward. Since the two boxes generally differ in size, ground-truth crops are resized to match the predicted-side dimensions via nearest-neighbor interpolation to preserve binary mask values. The clDice score is then computed on the shape-aligned patches using precomputed skeletons.

Hyperparameter Summary. Tab. 6 shows all reward hyperparameters for reproducibility.

8 Implementation Reference

We acknowledge the open-source codebases used in our implementation. For supervised fine-tuning, we build upon [38]. For GRPO training, we use EasyR1 [102], which is built on HybridFlow [75], and VLM-R1 [74].

Table 6: Reward function hyperparameters.

Parameter	Symbol	Value
<i>Top-level weights</i>		
Format weight	w_{fmt}	0.10
Accuracy weight	w_{acc}	0.85
Topological weight	w_{topo}	0.05
<i>Hungarian matching</i>		
Matching IoU threshold	τ_m	0.10
<i>Piecewise continuous IoU-to-score mapping ϕ</i>		
Tier thresholds	$\{\tau_k\}$	{0.3, 0.5, 0.7, 0.9}
Tier reward ceilings	$\{r_k\}$	{0.25, 0.55, 0.8, 1.0}
Smoothness exponent	γ	1.5
<i>clDice reward</i>		
Size threshold	τ_{sz}	0.30
Penalty scale	λ	0.80

9 Additional Experiments

We present additional experimental analyses that complement the main results in the paper. These experiments provide fine-grained breakdowns by error type, imaging domain, training stage, and sample complexity, offering deeper insight into the strengths and limitations of our approach.

Per-Error-Type Analysis. Tab. 7 reports detection F1 at IoU=0.5 for each of the four topological error types. Among the four categories, spurious connections are consistently the easiest to detect, likely because they introduce visually salient bridges between otherwise disjoint structures. In contrast, broken connections and extra branches remain more challenging, as they involve subtle, localized pixel-level changes. Notably, Topo-R1 achieves substantial improvements over SFT across all error types, with particularly large gains on the harder categories (e.g., broken connection improves from near-zero to over 30% F1), demonstrating that the topology-aware reward effectively steers the model toward fine-grained structural reasoning.

Per-Dataset Analysis. Tab. 8 breaks down detection performance across the four imaging domains in our benchmark. Performance varies across domains: road networks yield the highest F1, likely due to their higher contrast and simpler background, while retinal vasculature (OCTA-3M, OCTA-6M) and crack patterns present greater challenges owing to lower contrast and more complex morphology. Importantly, Topo-R1 consistently improves upon SFT across all domains, confirming that the topology-aware reward generalizes across structurally diverse imaging modalities.

Improvement Analysis. Tab. 9 quantifies the absolute improvement from SFT to Topo-R1 across three aggregate metrics. The reinforcement learning stage yields large and consistent gains for all backbone models, with the largest single improvement of +31.1 overall F1 observed for Qwen2.5-VL-3B. These results

Table 7: Detection F1 (%) by anomaly type at IoU=0.5. BC = Broken Connection, SC = Spurious Connection, MB = Missing Branch, EB = Extra Branch. Macro F1 is the unweighted average across all four types.

Model	Method	BC	SC	MB	EB	Macro
<i>Closed-Source Models (Zero-Shot)</i>						
GPT-4o	ZS	0.0	0.6	0.0	0.1	0.2
GPT-5.2	ZS	0.0	3.5	0.0	0.1	0.9
Gemini-2.5-Flash	ZS	0.1	4.2	0.1	0.0	1.1
Qwen3.5-VL-Plus	ZS	0.1	7.2	0.0	0.0	1.8
<i>Open-Source Models</i>						
InternVL-2.5-2B	ZS	0.0	0.0	0.0	0.0	0.0
	SFT	1.6	24.5	4.2	1.9	8.1
	Topo-R1	16.2	46.5	25.8	12.8	25.3
Qwen2.5-VL-3B	ZS	0.0	0.0	0.0	0.0	0.0
	SFT	0.6	36.9	1.0	0.7	9.8
	Topo-R1	30.3	61.8	42.2	22.0	39.1
Qwen3-VL-4B	ZS	0.0	0.0	0.0	0.0	0.0
	SFT	12.2	49.1	9.6	8.1	19.7
	Topo-R1	35.4	64.8	39.9	25.7	41.4
Qwen3-VL-8B	ZS	0.0	0.0	0.0	0.0	0.0
	SFT	3.2	49.9	3.5	8.0	16.2
	Topo-R1	31.9	66.0	36.3	27.9	40.5

confirm that SFT alone provides only a limited foundation, and that GRPO with our topology-aware composite reward is essential for achieving strong performance.

Effect of Error Complexity. Tab. 10 examines how detection performance scales with the number of ground-truth errors per sample. As expected, F1 decreases as the number of errors increases from single-error samples to complex multi-error scenes (6–10 errors), reflecting the increased difficulty of jointly localizing and classifying multiple anomalies. Nevertheless, Topo-R1 maintains substantially higher performance than SFT across all complexity levels, demonstrating robustness to varying error density.

Reward Component Ablation. Tab. 11 isolates the contribution of each reward component. The format reward R_{fmt} is retained in all configurations as it is necessary for parseable outputs. Removing the clDice reward (row 2) preserves strong detection and classification performance but degrades localization quality, as reflected by the drop in F1@0.75 and aF1. Conversely, removing the accuracy reward (row 3) substantially reduces the detection and classification metrics, since the model receives no explicit supervision to match predictions to ground-truth anomalies. The full composite reward (row 4) achieves the best performance across all metrics, confirming that both components provide complementary training signals.

10 Out-of-Distribution Results

OOD Test Set. To evaluate generalization under domain shift, we construct an out-of-distribution (OOD) test set of 1,564 samples from two retinal fundus

Table 8: Detection F1 (%) by dataset at IoU=0.5. The benchmark spans four imaging domains: road networks (Roads), retinal vasculature at two scales (OCTA-3M, OCTA-6M), and crack patterns (Crack).

Model	Method	Roads	OCTA-3M	OCTA-6M	Crack
<i>Closed-Source Models (Zero-Shot)</i>					
GPT-4o	ZS	0.1	0.1	0.3	0.1
GPT-5.2	ZS	0.5	1.3	1.4	0.3
Gemini-2.5-Flash	ZS	0.5	2.3	1.2	0.5
Qwen3.5-VL-Plus	ZS	0.7	3.4	2.0	0.8
<i>Open-Source Models</i>					
InternVL-2.5-2B	ZS	0.0	0.0	0.0	0.0
	SFT	11.9	12.2	10.1	7.3
	Topo-R1	42.6	28.8	25.3	25.0
Qwen2.5-VL-3B	ZS	0.0	0.0	0.0	0.0
	SFT	12.5	20.8	17.9	7.6
	Topo-R1	61.4	44.2	39.6	40.1
Qwen3-VL-4B	ZS	0.0	0.0	0.0	0.0
	SFT	34.5	30.6	26.8	17.4
	Topo-R1	63.8	43.9	40.0	43.5
Qwen3-VL-8B	ZS	0.0	0.0	0.0	0.0
	SFT	23.7	29.5	26.9	14.0
	Topo-R1	63.9	43.4	39.8	41.1

Table 9: Absolute improvement (Δ) from SFT to Topo-R1. F1 (%) at IoU=0.5 for overall, macro (unweighted per-type average), and COCO aF1.

Model	Overall F1@0.5		Macro F1@0.5		aF1 (COCO)	
	SFT	Δ	SFT	Δ	SFT	Δ
InternVL-2.5-2B	9.0	+23.0	8.1	+17.2	4.0	+13.1
Qwen2.5-VL-3B	11.9	+31.1	9.8	+29.3	5.3	+16.1
Qwen3-VL-4B	23.0	+22.2	19.7	+21.7	12.8	+11.9
Qwen3-VL-8B	20.2	+23.7	16.2	+24.3	11.8	+12.5

Table 10: Detection F1 (%) by anomaly complexity at IoU=0.5. Samples grouped by ground-truth anomaly count: single (n=833), 2-5 (n=1712), 6-10 (n=835). Topo-R1 maintains strong performance on complex multi-anomaly samples.

Model	Method	Single	2-5	6-10
InternVL-2.5-2B	SFT	18.8	9.7	7.8
	Topo-R1	35.8	32.4	25.3
Qwen2.5-VL-3B	SFT	13.8	12.8	11.1
	Topo-R1	47.6	47.1	38.2
Qwen3-VL-4B	SFT	33.2	25.5	19.4
	Topo-R1	53.7	49.0	40.1
Qwen3-VL-8B	SFT	29.3	21.8	17.5
	Topo-R1	53.5	47.3	38.7

vessel segmentation datasets unseen during training: DRIVE [78] (200 samples, 12.8%) and HALVS [50] (1,364 samples, 87.2%). Each sample consists of an image patch paired with either the corresponding ground-truth segmentation mask or a corrupted segmentation mask generated by synthetically injecting topological errors into the ground-truth annotations. The samples are organized into

Table 11: Reward component ablation on Qwen3-VL-4B. Format reward R_{fmt} is always enabled. R_{acc} : accuracy reward; R_{topo} : cLDice reward. All metrics in %; best per column in bold.

R_{fmt}	R_{acc}	R_{topo}	Detection		Classification	Localization	
			F1@0.5	aF1	Macro F1@0.5	F1@0.75	mPS-F1@0.5
✓	×	×	25.1	13.4	20.8	12.6	39.2
✓	✓	×	43.8	23.5	39.7	20.1	56.8
✓	×	✓	31.4	17.6	26.3	17.8	44.1
✓	✓	✓	45.2	24.7	41.4	22.5	58.5

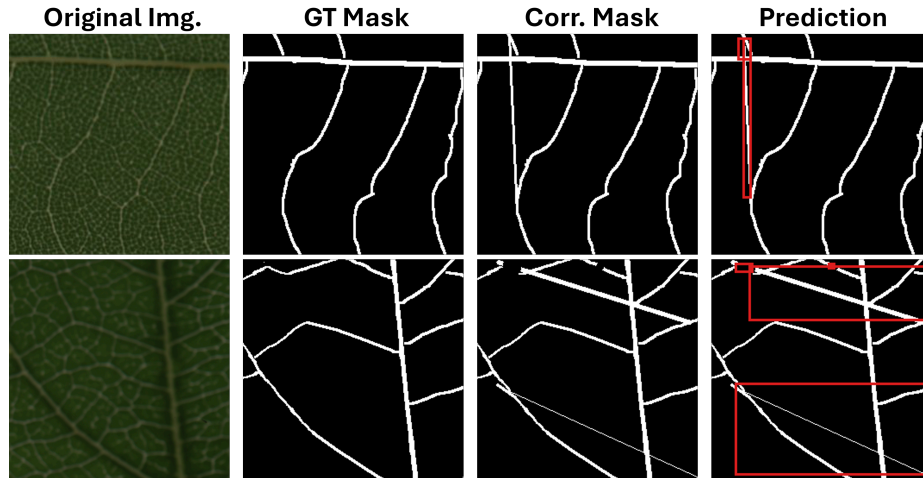


Fig. 6: Out-of-distribution qualitative results on leaf venation networks. Topo-R1 generalizes to an unseen domain (leaf veins) and correctly detects topological anomalies, such as broken and spurious connections, in the corrupted masks. Red boxes denote predicted error regions.

three tiers: no-error (314, 20.1%), single-error (312, 19.9%), and multi-error (938, 59.8%, containing 2-10 errors per mask). Across all samples, a total of 4,915 error instances are nearly uniformly distributed over four types: broken connection (25.1%), spurious connection (25.0%), missing branch (25.0%), and extra branch (24.9%), yielding an average of 3.14 instances per sample. The OOD set differs from the training distribution in both the imaging domain (different protocols, resolutions, and vessel appearances) and the annotation source (independent annotators), making it a rigorous benchmark for assessing topological anomaly detection under real-world distribution shift.